

OPEN

Multi-band MIM refractive index biosensor based on Ag-air grating with equivalent circuit and T-matrix methods in near-infrared region

Mohamad Nejat & Najmeh Nozhat*

In this paper, a multi-band metal-insulator-metal (MIM) perfect absorber with refractive index sensing capability has been investigated in near-infrared region. The proposed structure has been studied for biomedical applications such as detection of solution of glucose in water, diagnosis of different stages of malaria infection, bacillus bacteria and cancer cells. The MIM configuration improves the sensing parameters of the biosensor due to the good interaction with the analyte. The high sensitivity and figure of merit of 2000 nm/RIU and 100 RIU⁻¹ have been achieved, respectively. Also, the Ag-air grating in the suggested plasmonic sensor helps the localized surface plasmons excitation and makes the structure sensitive to the incident lightwave polarization. Therefore, the presented biosensor behaves like a polarization switch with the high extinction ratio and fast response time of 25.15 dB and 100 fs, respectively. The methods of equivalent circuit model and transmission matrix have been utilized to verify the simulation results, as a new challenge in near-infrared region. The new idea of multi-application plasmonic devices, the feasibility of fabrication for the presented structure and utilizing mentioned analytical methods in near-infrared region could pave the way for the future of plasmonic structures.

Surface plasmons (SPs), which are created by the interaction between the free electrons of metal and incident electromagnetic wave at metal-dielectric interfaces, have two kinds of localized surface plasmons (LSPs) and propagating surface plasmons (PSPs)¹. While LSPs only oscillate on their own place, PSPs propagate in the form of an oscillating charge wave due to the large enough interface of the metallic layer². Today, the theory of surface plasmon resonance (SPR) has been used in a lot of optical studies about food safety testing³, environmental monitoring⁴, medical diagnosis⁵, optical bistability⁶, surface-enhanced Raman spectroscopy (SERS)⁷, and second harmonic (SH) generation⁸. Subwavelength structures with metal films, which usually form a nanocavity, allow the hybridization of the cavity resonance modes with the LSP modes². Overcoming the diffraction limit and field enhancement are other benefits of plasmonic structures⁹.

Over recent years, many SP-based structures have been studied and investigated such as perfect absorbers¹⁰, waveguides¹¹, modulators¹², lasers¹³, and sensors¹⁴. The unique properties of the SPRs such as strong dependency on the size, geometrical shape and refractive index of the surrounding medium make them good candidates for sensing applications¹⁵.

It is well known that the sensing performance of SPR-based sensors is due to the wavelength shift ($\Delta\lambda$) of the response spectrum, when the refractive index of the test medium (Δn) changes. The sensitivity ($S = \Delta\lambda/\Delta n$), full-width at half-maximum (FWHM) and figure of merit ($FOM = S/FWHM$) are the main parameters for evaluating the sensing performance^{14,16}. SPR-based sensors have attracted much attention because of good advantages like miniaturization, rapid response and high sensitivity¹⁷. Moreover, they have a key role in detection of bacteria¹⁸, proteins¹⁹, DNA²⁰, RNA²¹, viruses²², analytes²³, and chemical and biological species²⁴.

Widespread applications such as food quality control, health, diseases diagnosis, and environmental and molecular monitoring make the biosensors a hot topic for researchers in these years²⁵⁻²⁷. The label-based and label-free sensors are two main types of biosensors. The first one has lower reliability than the second one because it can change the molecule's binding properties. The label-free biosensors, which have advantages such as real

Department of Electrical Engineering, Shiraz University of Technology, Shiraz, 7155713876, Iran. *email: nozhat@sutech.ac.ir

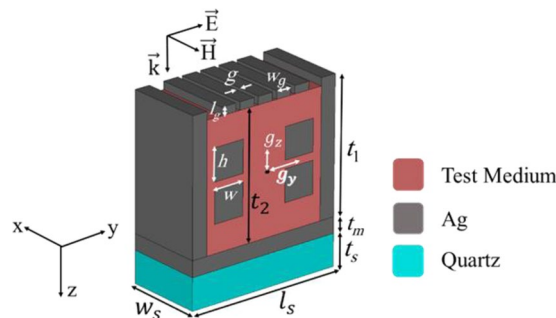


Figure 1. The schematic view of a unit cell of the proposed biosensor.

time monitoring without any label, operate like other SPR-based sensors and detect the refractive index variation of the test medium²⁸. Label-free detection, direct and rapid response, spectral tunability, strong enhancement of local electric field, and adaptability to modern nanotechnology architectures are some of the remarkable benefits of the SPR-based label-free biosensors that have been widely studied for medical applications^{28,29}.

Sun *et al.* have suggested a plasmonic sensor based on Mach-Zehnder interferometer with a double-slot hybrid plasmonic waveguide and the high sensitivity of 1061 nm/RIU has been attained³⁰. Also, a horizontal slot waveguide biosensor for detection of DNA hybridization with the sensitivity of 893.5 nm/RIU has been investigated³¹. Another label-free plasmonic biosensor has been studied by Hameed *et al.*²⁸. Their suggested structure consists of a hybrid plasmonic slot waveguide based on silicon-on-insulator (SOI) and the high sensitivity of 1890.4 nm/RIU has been achieved for detection of DNA hybridization. Another group of plasmonic sensors are metamaterial based ones. Kabashin *et al.* have presented a metamaterial based plasmonic sensor for biosensing applications³². They have illustrated an improvement in biosensing technology using a plasmonic metamaterial, which supports a guided mode in a porous nanorod layer. Moreover, a microfluidic sensor for dielectric characterization has been studied and presented in ref. ³³. The proposed sensor consists of a split ring resonator, which can help the use of microfluidic sensors for identification, classification, and characterization of chemical and biochemical analytes.

There are different methods to excite SPs in plasmonic structures. The nanoparticle usage for LSPs excitation is the primary method¹. It is worth noting that according to the definition of LSPs, an arbitrary dielectric-metal interface with smaller length than the resonance wavelength can provide a context in which the excitation of LSPs occurs. Prism-coupling, waveguide-coupling, and grating-coupling are some well-known methods for PSPs excitation. A conventional plasmonic structure for PSPs excitation is Kretschmann configuration, which has a thin metal layer coated over the base of a prism³⁴. For a long time, the Kretschmann structure has been studied and commercialized, but the need for the prism makes it bulky. Therefore, a compact and portable sensor with the ability of integration with other plasmonic devices is needed. The grating-based plasmonic structure that has been studied in many researches can satisfy the mentioned requirements^{9,35}.

Metal-insulator-metal (MIM) configuration which has been utilized former in many structures such as waveguides, filters, switches and interferometers can enhance the sensing performance of plasmonic sensors¹⁷. For example, Xie *et al.* have suggested a plasmonic sensor based on MIM waveguide with side-coupled hexagonal cavity³⁶. They have achieved the high sensitivity of 1562.5 nm/RIU and good FOM of 38.6 RIU⁻¹ at $\lambda = 1550$ nm.

In this paper, a hybrid plasmonic four-band perfect absorber has been investigated as a biosensor for detection of malaria infection, cancer cells, bacillus bacteria, and 25% solution of glucose in water in near-infrared region. First, the design procedure of the multi-band absorber with sensing capability has been studied based on the MIM configuration and Ag-air grating. Then, the effects of geometrical parameters on the absorption and sensing performances, the physical insight of perfect absorption and the fabrication process have been investigated. Also, two analytical methods of equivalent circuit model and transmission (*ABCD*) matrix have been utilized to verify the simulation results. Moreover, the switching performance of the proposed structure has been shown. Here, our new idea of multi-application plasmonic devices has been utilized to have sensing and switching performances in the designed structure, simultaneously. The achievements can pave the way for utilizing two mentioned analytical methods to validate the simulation results of any arbitrary plasmonic structure at near-infrared wavelengths. In addition, the good performances of our proposed structure in sensing and switching capabilities can open a new window for development of plasmonic applications.

Design and Simulation Results of Four-band Perfect Absorber with Sensing Performance

A unit cell of the proposed structure that is composed of a dielectric substrate, a layer of silver (Ag) and silver walls is depicted in Fig. 1. The Ag walls help the perfect absorption of the structure by trapping the incident lightwave and causing more SPRs. More importantly, these walls provide a context in which the fluid test substance can cross in the designated path. To have good interaction with the analyte, four Ag cubic resonators are located inside the suggested sensor, where is filled with the test material. The arrangement of the Ag cubic resonators and other parts of the structure causes the MIM coupling effect in the presented structure. Also, an Ag-air grating with the period of $w_g + g = 130$ nm is used on top of the structure to help the SPs excitation, when the incident lightwave impinges on the structure.

Parameter	Value (nm)	Parameter	Value (nm)
w_s	500	g_y	250
l_s	1010	g_z	125
t_s	200	h	200
t_m	100	w	200
t_1	850	l_g	50
t_2	800	w_g	100

Table 1. The values of the geometrical parameters of the proposed four-band biosensor.

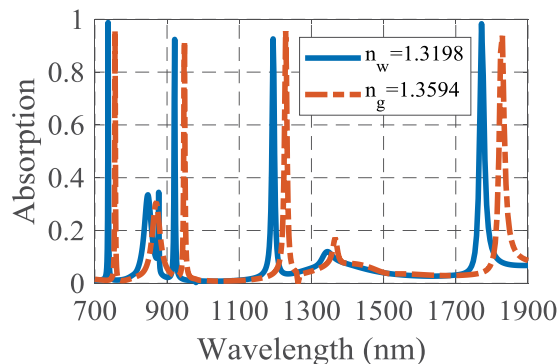


Figure 2. The absorption spectra of the suggested biosensor when the analyte refractive index changes for detection of 25% solution of glucose in water.

The dielectric layer is quartz with the permittivity of $\epsilon_r = 2.25$ and the silver is modeled according to the Johnson and Christy data^{37,38}. The absorption coefficient (A) can be given by³⁹:

$$A = 1 - R - T \quad (1)$$

where T and R are the transmission and reflection coefficients, respectively.

The CST Microwave Studio software has been used to perform the full-wave simulation based on the three dimensional (3D) finite element method (FEM) with open boundary condition along the z direction and periodic boundary condition along the x and y directions. The open boundary condition is one of the most useful boundary conditions in this software which has been used along the direction of the incident lightwave (z -axis) to provide the stimulation conditions and consequently the source can be applied in this direction. The tetrahedral mesh in the frequency domain with the size of 10 tetrahedrons per wavelength has been utilized to calculate the scattering parameters and absorption spectrum according to Eq. (1). All the remained parameters in the simulation are selected as the default setting of the software.

When an electromagnetic wave illuminates the structure from the top, it will be trapped in the absorber, since the thickness of the Ag layer is larger than its skin depth in near-infrared region ($T = 0$). The y -polarized incident wave excites the SPs by means of the Ag-air grating. The SPs excitation and the MIM coupling help the perfect absorption by absorbing the energy of the incident lightwave. Consequently, by selecting the values of the geometrical parameters according to Table 1, the structure can behave as a multi-band perfect absorber, as it will be shown.

According to the dependency of SPRs properties on the surrounding medium, a change in the refractive index of the analyte results in a change in the absorption spectrum of the structure. Here, the absorption spectrum experiences a wavelength shift by changing the refractive index of the test medium from $n_w = 1.3198$ to $n_g = 1.3594$, as shown in Fig. 2.

The proposed structure has four near-unity absorption peaks at the wavelengths of 745, 935, 1207.5 and 1800 nm. The sensitivity and FOM of the presented biosensor are 479.79, 686.86, 878.78 and 1457.57 nm/RIU and 239.89, 171.71, 109.84 and 85.71 RIU⁻¹, respectively, for the four mentioned wavelengths. It is noteworthy that n_w and n_g are the refractive indices of water and 25% solution of glucose in water, respectively². Here, the four near perfect absorption are due to the MIM configuration and SPs excitation by utilizing the cubic resonators and Ag-air grating, and also proper values for geometrical parameters of the structure. The physical insight of the light absorption will be discussed explicitly in the following.

The variation of the sensitivity and FOM at the resonance wavelengths is illustrated in Fig. 3. It should be noticed that the resonance modes of the structure are decreased by increasing the operating wavelength as a result of the cavity behavior of the structure. Therefore, the sensitivity is improved for higher wavelengths, in which the structure has few resonances and all the absorbed electromagnetic energy contributes to the stronger resonance. However, the loss of the structure is increased and hence the FOM is decreased. In contrast, at lower wavelengths the structure has more resonance modes and so the incident wave energy is divided between more resonance

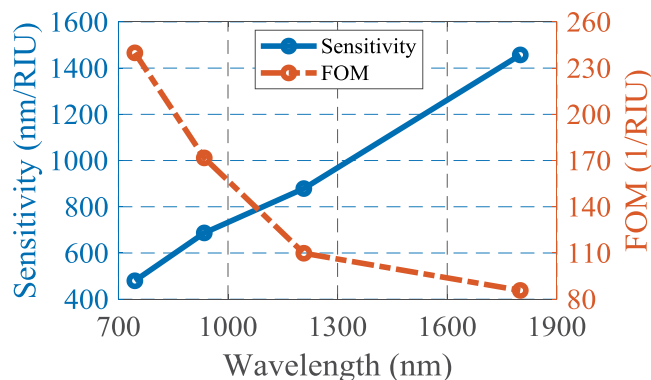


Figure 3. The sensing parameters of the proposed structure at resonance wavelengths.

modes and the strength of resonance and sensitivity are decreased. It is obvious that the energy of the incident lightwave for each resonance mode has a particular value.

To have a better insight of the cubic resonators effect, we have considered the same structure of Fig. 1 with two resonators while the structural parameters are the same as Table 1. The proposed structure of Fig. 4(a) does not have good resonances due to the large distance between the resonators and other metallic parts of the structure. In this case, the structure has only one perfect absorption peak at $\lambda = 900$ nm with the sensitivity of 546.71 nm/RIU, as shown in Fig. 4(b). In the second case, the structure of Fig. 1 with six cubic resonators has been considered, as depicted in Fig. 4(c). Since the resonators are so close to each other, the LSPs interaction with the analyte and the sensitivity are enhanced compared to the former state. But, the analyte portion is decreased and the sensitivity is not as good as Fig. 1. According to the absorption spectrum of Fig. 4(d) the sensitivity is obtained as 689.39 nm/RIU at $\lambda = 1100$ nm. Many other arrangements like Fig. 4(e) have been also simulated and studied. But, as shown in Fig. 4(f), there is no enhancement in the absorbing and sensing performances and the multi-band behavior of the structure is diminished. In this state, the best sensitivity and FOM are 1401.51 nm/RIU and 202.02 RIU⁻¹, respectively. The achieved sensing parameters in this state are lower than the reported values for Fig. 1. Therefore, the geometrically optimized structure of Fig. 1 has been chosen in the following. Moreover, the space between the resonators has been tuned by changing the parameters of g_x and g_y and the optimized values have been selected and reported in Table 1.

Here, the effect of Ag-air grating has been investigated. As mentioned before, the grating helps the SPs excitation and the absorption diminishes without the grating, as shown in Fig. 5. It is considerable that the resonances in this case are partly because of the four cubic resonators.

To better understand the effect of MIM configuration and coupling of metallic parts, the test medium thickness (t_2) has been tuned when the other parameters are remained constant. Increasing t_2 results in an increase in the portion of analyte in the structure. Since the proposed structure behaves like a cavity, increasing t_2 leads to improving the sensing performance by providing more space for more resonances and so more interaction between the test medium and excited SPs in the structure. But, as shown in Fig. 6, further increase of the test medium thickness decreases the sensitivity and FOM, due to the less MIM coupling as a result of further gap between the metal parts of the structure. To have good sensing performance t_2 is selected as 800 nm for the following simulations.

Moreover, the effects of the length (h) and width (w) of the cubic resonators on the absorbing performance have been studied. According to Fig. 7, it is obvious that increasing the dimensions of the resonators causes a redshift in the resonance wavelength. Since h is orthogonal to the electric field of the incident lightwave and the LSPs are almost excited in this interface of metallic cubic resonators and test medium¹⁴, changing the value of h has more effect on the absorption spectrum compared to the variation of w . The dimensions of cubic resonators have been chosen 200×200 nm² to create good absorption with proper resonance wavelength.

The dielectric substrate has been utilized for fabrication feasibility and it does not affect the absorption spectrum, when the Ag layer thickness is more than its skin depth at the desired wavelengths. Therefore, t_s does not have any effect on the absorbing and sensing performances, as shown in Fig. 8.

Figure 9 demonstrates the E-field distribution ($|E_z|$) of the proposed structure for four wavelengths of 745, 935, 1207.5 and 1800 nm. The excitation and interaction of LSPs, which are due to the MIM configuration and Ag-air grating, can be seen in this figure. The MIM coupling of the structure, which has a key role in the performance of the biosensor, causes a good interaction with the test medium as an insulator in the MIM configuration. The cubic shape has been selected for resonators because of the concentration of surface charges at the corners to make the coupling stronger. To have better insight, the MIM parts of the presented structure have been written on Fig. 9. The cubic resonators and the Ag walls and layer are the metal parts, and the test medium is considered as the dielectric part of the structure. Furthermore, all the above mentioned help the perfect absorption performance at four resonance wavelengths. It is obvious from Fig. 9 that the incident lightwave traps in the structure by means of SPRs and good interaction of LSPs which are shown as concentrated E-field distribution at the desired wavelengths.

The fabrication feasibility of the proposed structure has been considered in our design process and consequently some dielectric parts have been added to keep the cubic resonators and make the structure feasible for fabrication. Also, a 50 nm dielectric layer with the refractive index of $n = 1.4$ which can be replaced by LiF in this

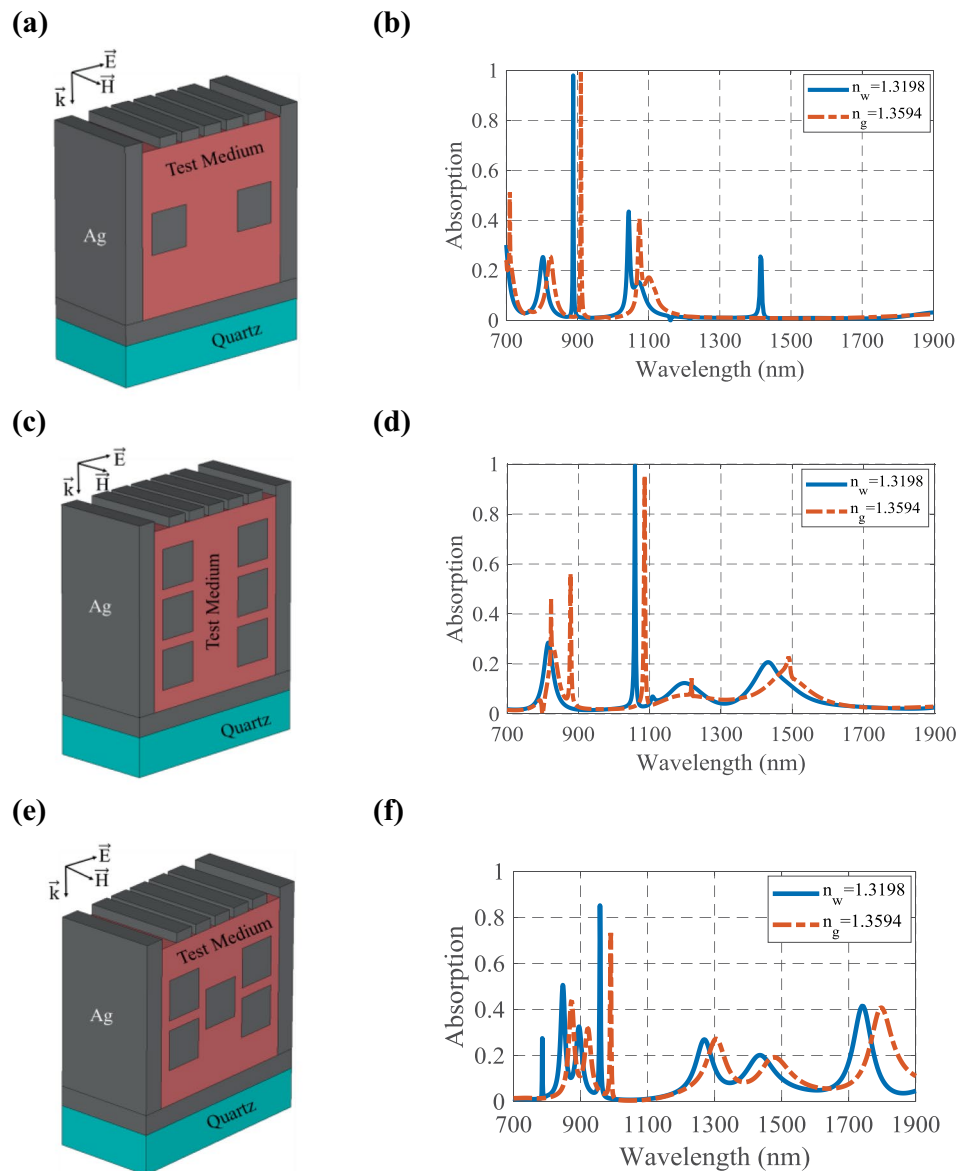


Figure 4. The proposed structure with (a) two cubic resonators, (c) six cubic resonators, and (e) five cubic resonators. The absorption spectra of the biosensor with (b) two cubic resonators, (d) six cubic resonators, and (f) five cubic resonators, when the refractive index changes from $n_w = 1.3198$ to $n_g = 1.3594$.

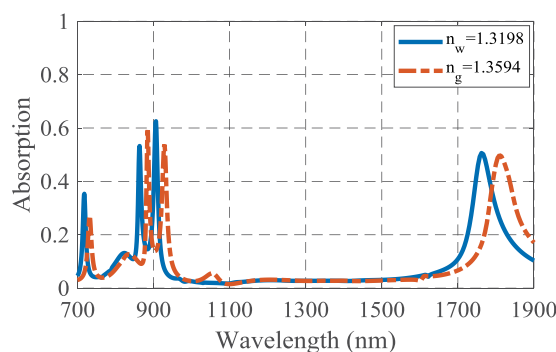


Figure 5. The absorption spectrum of the proposed biosensor without the Ag-air grating for detection of 25% solution of glucose in water.

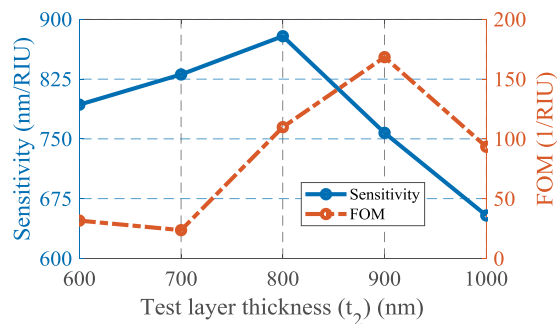


Figure 6. The effect of the test layer thickness on the sensing parameters of the proposed biosensor.

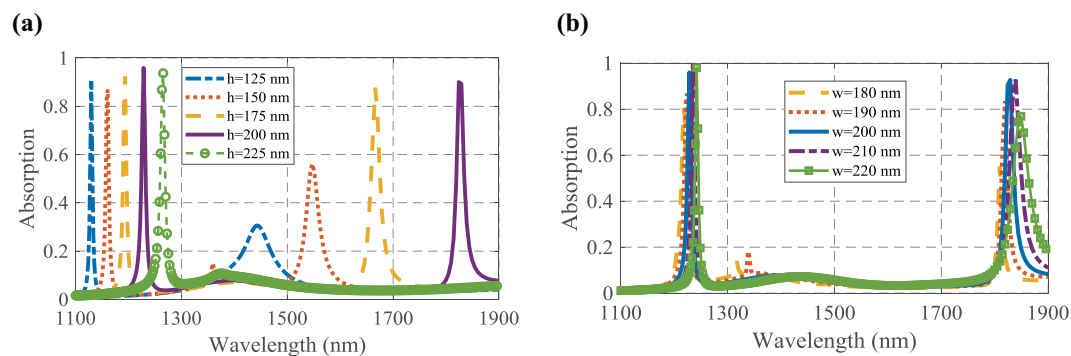


Figure 7. The effects of the (a) length and (b) width of the resonators on the absorbing function of the proposed biosensor, when the analyte refractive index is 1.3594.

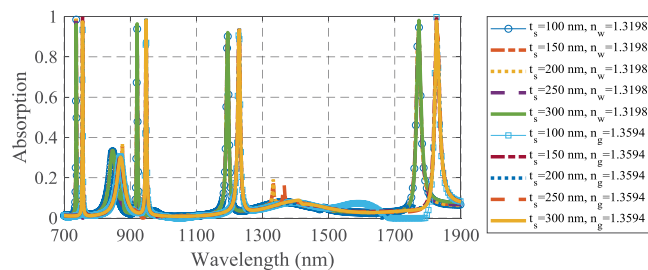


Figure 8. The absorption spectra of the suggested biosensor for different values of the substrate thickness.

wavelength range⁴⁰, has been placed under the grating layer to prevent the suspension of Ag-air grating, as shown in Fig. 10(a). The effect of the width of the dielectric parts on the absorption spectrum has been also studied in Fig. 10(b) and observed that the added dielectric parts have no significant effect on the performance of the proposed structure.

The fabrication process of the proposed structure of Fig. 10(a) can be described as follows. At first, an Ag layer with the thickness of t_m is evaporated on a 200 nm quartz layer. Then, the process goes on with depositing other layers from bottom to top, as shown in Fig. 11(a). According to Fig. 11(b), by means of a mask, deep UV stepper and reactive ion etching (RIE), when a photoresist is placed above the structure, the proposed shape of Fig. 11(c) can be obtained through the lithography method. Afterwards, the test medium of Fig. 10(a) is filled with photoresist as a sacrificial layer and a 50 nm dielectric layer is deposited above the structure, as shown in Fig. 11(d). Next, as depicted in Fig. 11(e), the desired grating and Ag walls are grown and patterned on the top and sides of the structure utilizing lithography and etching. Finally, the sacrificial layer can be removed through the acetone to have the structure of Fig. 11(f).

The Biomedical Applications of the Proposed Plasmonic Sensor

In this section, the sensing parameters of the proposed plasmonic refractive index sensor in biomedical applications have been investigated. As it was mentioned before, the 25% solution of glucose in water changes the refractive index of water from $n_w = 1.3198$ to $n_g = 1.3594$ ⁴¹. According to ref. ⁴¹, different stages of malaria infection decrease the refractive index of a healthy red blood cell that is 1.4. Ring, trophozoite and schizont are three stages

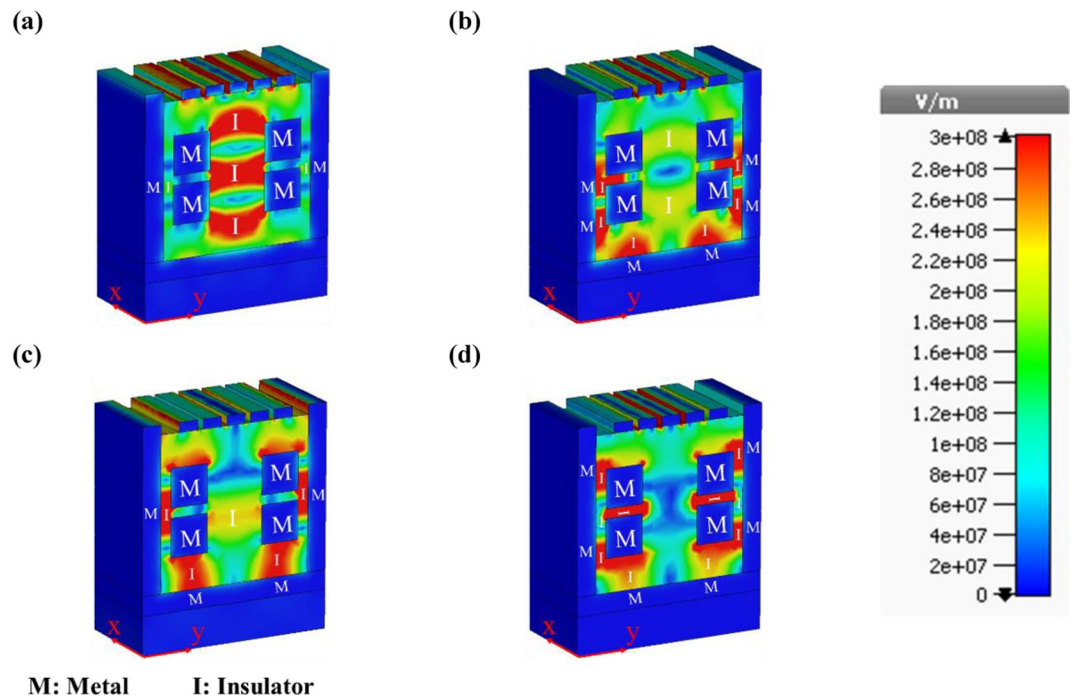


Figure 9. The E-field distributions of the suggested plasmonic sensor at the wavelengths of (a) $\lambda = 745$ nm, (b) $\lambda = 935$ nm, (c) $\lambda = 1207.5$ nm, and (d) $\lambda = 1800$ nm.

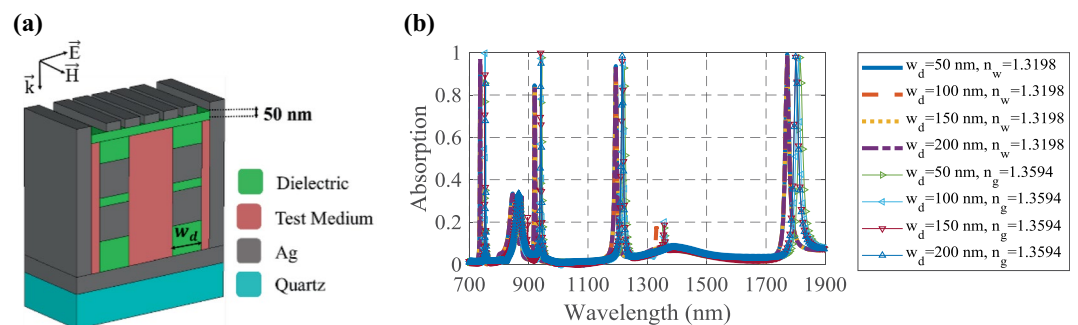


Figure 10. (a) The schematic view and (b) the absorption spectra of the proposed structure with added dielectric parts.

of malaria infection. Based on the simulation results, our suggested biosensor has the high sensitivity of 2000 nm/RIU and high FOM of 100 RIU⁻¹ for detection of the first stage of malaria infection, which can be so useful for quick treatment of infected people. It is considerable that 250 million people are affected by malaria annually⁴¹. The bacillus bacteria change the average refractive index of a healthy cell from 1.4 to 1.539. Also, the cancer cells have higher refractive index of 1.370 than the healthy cells (1.353)⁴¹. The sensing parameters of the proposed biosensor for all mentioned applications are listed in Table 2.

Analytical Methods

The simulation results of the proposed biosensor can be evaluated by analytical methods. The equivalent circuit model is the first method that is utilized to verify the simulation results. The dielectric substrate is modeled by the transmission line 1 (TL-1) with the characteristic impedance of $Z_s = \eta_0 / \sqrt{\epsilon_r}$, the propagation constant of $\beta_s = 2\pi / \lambda_g$, and the electrical length of $E_s = 2\beta_s t_s$, where η_0 , ϵ_r , and λ_g are the free space impedance, the relative permittivity of the dielectric layer, and the guided wavelength, respectively¹⁴. Also, the test medium, modeled by the transmission line 2 (TL-2), has the same parameters of the TL-1, in which ϵ_r should be replaced by $\epsilon_a = n_{analyte}^2$.

The parallel branches that consist of different elements are used to model the MIM and grating configurations, as shown in Fig. 12(a). The Ag impedance can be calculated through the well-known formula⁴²:

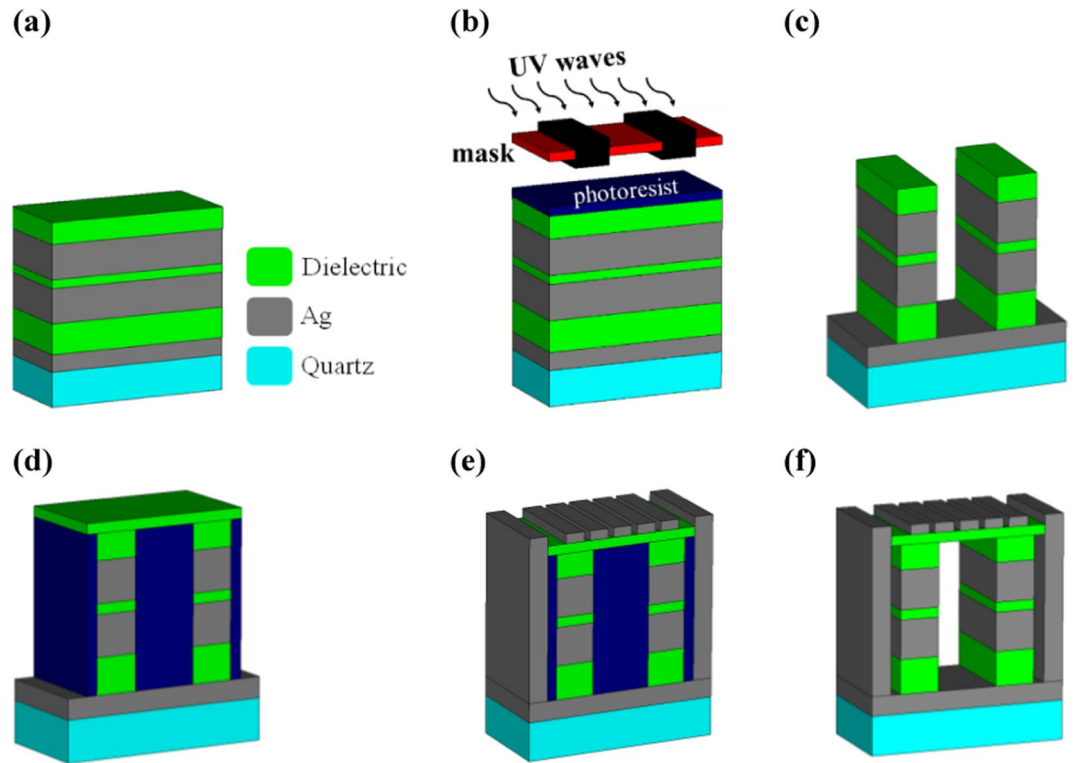


Figure 11. Schematic view of the fabrication process of the suggested plasmonic sensor.

The test material		Refractive index	S (nm/RIU)	FOM (RIU ⁻¹)
25% solution of glucose in water		$n_w = 1.3198,$ $n_g = 1.3594$	1457.07	85.71
Malaria infection	Ring stage	$n_1 = 1.4,$ $n_2 = 1.395$	2000	100
	Trophozoite stage	$n_1 = 1.4,$ $n_2 = 1.383$	1523.53	67.17
	Schizont stage	$n_1 = 1.4,$ $n_2 = 1.373$	1344.44	67.22
Bacillus bacteria		$n_1 = 1.4,$ $n_2 = 1.539$	876.26	43.81
Cancer cells		$n_1 = 1.353,$ $n_2 = 1.370$	1407.59	77.40

Table 2. The sensing parameters of the proposed plasmonic sensor in biomedical applications.

$$Z_{Ag} = R_{Ag} + j\omega L_{Ag} = \sqrt{\frac{\omega\mu}{2\sigma}}(1 + j) \tag{2}$$

where σ and μ are the conductivity and permeability of the metallic layer, respectively.

The second analytical method is the transmission (ABCD) matrix. In this case, the T-matrix of each element of the equivalent circuit is extracted and calculated. The T-lines of the substrate and test medium can be modeled with $T_s = \begin{bmatrix} \cos(\beta_s t_s) & jZ_s \sin(\beta_s t_s) \\ j \sin(\beta_s t_s)/Z_s & \cos(\beta_s t_s) \end{bmatrix}$ and $T_a = \begin{bmatrix} \cos(\beta_a t_a) & jZ_a \sin(\beta_a t_a) \\ j \sin(\beta_a t_a)/Z_a & \cos(\beta_a t_a) \end{bmatrix}$, respectively⁴³. The shunt and series branches of the circuit model have the T-matrices of $T_{shunt} = \begin{bmatrix} 1 & 0 \\ 1/Z_{shunt} & 1 \end{bmatrix}$ and $T_{series} = \begin{bmatrix} 1 & Z_{series} \\ 0 & 1 \end{bmatrix}$, respectively⁴³. The transmission matrix of the whole structure can be achieved by cascading the T-matrix of each section. Therefore, the scattering parameters and optical response of the T-matrix model can be obtained by⁴³:

$$R = |S_{11}|^2 = \left| \frac{A + B/\eta_0 - C\eta_0 - D}{A + B/\eta_0 + C\eta_0 + D} \right|^2 \tag{3}$$

where A, B, C and D are the elements of the main T-matrix of the proposed structure.

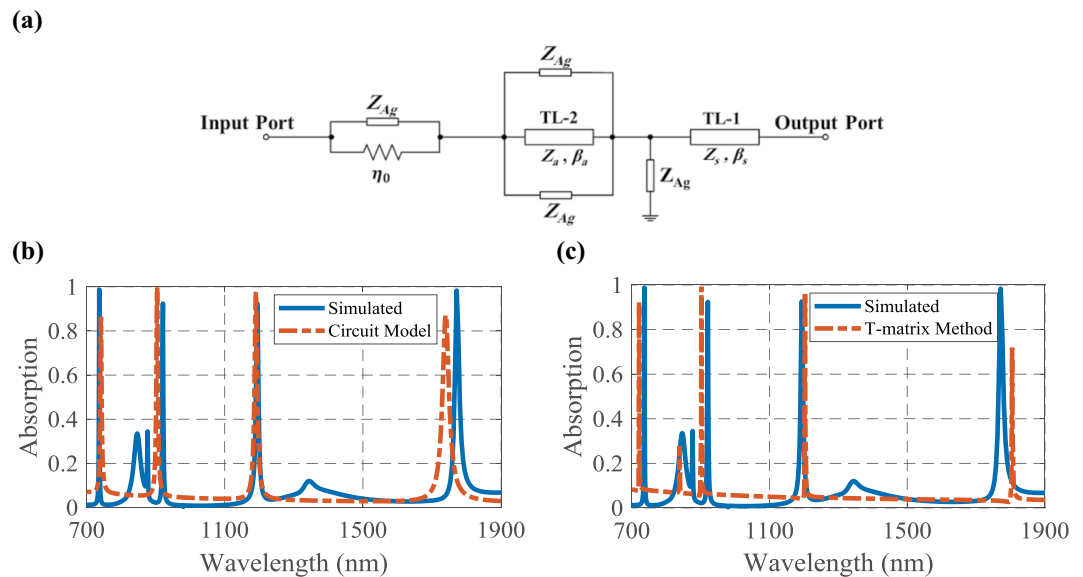


Figure 12. (a) The equivalent circuit model of the proposed four-band perfect absorber, the comparison between the simulated and analytical methods of (b) equivalent circuit model and (c) T-matrix.

Parameter	Value	Parameter	Value
Z_s	251.32(Ω)	$E_s = 2\beta_s t_s$	132.51°
Z_a	285.64(Ω)	$E_a = 2\beta_a t_a$	524.68°
R_{Ag}	35(Ω)	L_{Ag}	0.4(fH)

Table 3. The Parameters values of the analytical methods.

The extracted circuit model is simulated in the Advanced Design System (ADS) software to calculate the scattering parameters. By setting the values of Table 3, the absorption spectrum of the suggested biosensor according to the mentioned analytical methods is calculated through Eq. (1).

As shown in Fig. 12(b,c), both analytical methods have good agreement with the simulation results for four resonance wavelengths. Since the dielectric layers of the structure have been modeled by the T-lines, the electrical lengths of the T-lines affect the scattering parameters of the extracted model and the absorption spectra of Fig. 12. The results of the analytical methods can be tuned through the optimization and changing the values of the extracted parameters of Table 3 around their initial values. Therefore, the absorption spectra of the analytical methods can be changed to have more resonances and match with all resonance wavelengths of the simulation results. But, the absorption value may be diminished. Therefore, there is a trade-off between the resonance wavelengths and their absorption values. Here, we have focused on the four resonance wavelengths that their sensing performance have been considered and so in the extracted circuit model we have tried to match these four resonance wavelengths well.

The Switching Capability of the Proposed Biosensor

According to the design procedure, the presented structure can be illuminated by an incident lightwave with y-polarized E-field, which is perpendicular to the Ag-air grating. Consequently, the change of incident wave polarization from y- to x-axis changes the performance of the absorber and leads to total reflection of the incident wave. Therefore, the absorption coefficient becomes near-zero for the whole wavelength range of 700 to 1900 nm, as depicted in Fig. 13. This figure shows the switching capability of the proposed biosensor from “ON” to “OFF” state.

The response time of the suggested plasmonic switch can be calculated by applying a continuous wave (CW) at the resonance wavelength to the structure and time monitoring of the output port, when the output signal approaches the steady state. The process of changing the incident lightwave polarization does not be considered in calculation of the response time. Another main parameter of a plasmonic switch is extinction ratio that exhibits the difference between the absorption values in “ON” and “OFF” states³⁷:

$$\eta(\text{dB}) = 10 \log \left(\frac{A_{on}}{A_{off}} \right) \quad (4)$$

To have a better insight of simultaneous sensing and switching performances of the presented perfect absorber, the parameters of both capabilities for detection of glucose in water are listed in Table 4.

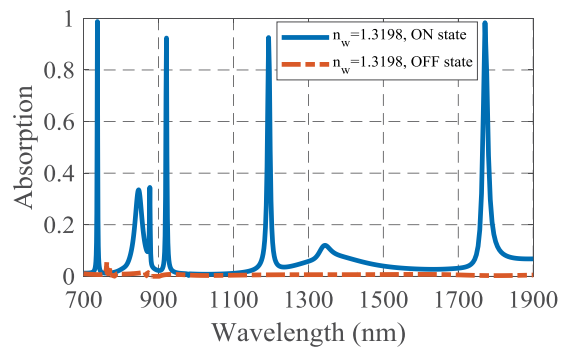


Figure 13. The absorption spectra of the proposed plasmonic biosensor for “ON” and “OFF” states when the electric field polarization changes from y - to x -axis, respectively.

λ (nm)	S (nm/RIU)	FOM (RIU ⁻¹)	η (dB)	Response time (fs)
745	479.79	239.89	21.50	180
935	686.86	171.71	21.20	170
1207.5	878.78	109.84	21.88	150
1800	1457.07	85.71	25.15	100

Table 4. The sensing and switching performances of the proposed biosensor for detection of glucose in water.

Reference	S (nm/RIU)	FOM (RIU ⁻¹)	λ (nm)	η (dB)	Response Time (fs)
28	1890.4	—	1535.7	—	—
30	1061	—	1554	—	—
31	893.5	—	1550	—	—
36	1562.5	38.6	1550	—	—
44	557	6.1	1000	—	—
45	503	63	930	—	—
46	223	19.5	1170	—	—
47	250	28	1100	—	—
48	600	28	1100	—	—
49	1100	224	1000	—	—
50	1200	15	1550	—	—
37	—	—	1550	9.27	—
51	—	—	1550	13.96	90
52	—	—	1550	11.14	—
53	—	—	1550	14.36	—
54	—	—	1550	20	14e9
This work	2000	100	1880	22.13	200
	1457.07	85.71	1800	25.15	100

Table 5. Comparison of the sensing and switching performances of our proposed biosensor with other reported plasmonic sensors and switches.

Our suggested biosensor has the capabilities of sensing and switching, simultaneously. To the best of our knowledge, there is not any reported plasmonic structure with two mentioned abilities in one designed structure. Therefore, our proposed structure is compared with the plasmonic sensors and switches in near-infrared region, separately. Table 5 shows the comparison between the performances of our suggested structure with previous works. Some reported structures may have high sensitivity or FOM in sensing performance and high extinction ratio or fast response time in switching performance, but not simultaneously. In contrast, our suggested structure not only has two capabilities, simultaneously, but also has high sensing and switching performances.

Conclusion

In summary, we have investigated a plasmonic biosensor with switching capability in near-infrared region. The suggested structure has the high sensitivity of 2000 nm/RIU and high FOM of 100 RIU⁻¹ due to the MIM coupling and interaction between the Ag cubic resonators and test medium. The simulation results show the ability of the proposed plasmonic sensor in detection of glucose in water, diagnosis of malaria infection, bacillus bacteria

and cancer cells. The Ag-air grating, which has been used to excite the SPs in the plasmonic sensor, helps the structure to have switching capability with high extinction ratio of 25.15 dB and fast response time of 100 fs. Therefore, the implemented structure has better performance than the other reported plasmonic sensors and switches in two considered capabilities of sensing and switching, simultaneously. The simulation results have been validated by two analytical methods. The equivalent circuit model and T-matrix methods are two utilized analytical methods, which have been used in near-infrared region in this work. The multi-application idea of this manuscript, considering the fabrication feasibility and verifying the simulated results with analytical methods can be used for plasmonic devices in the future.

Received: 6 February 2020; Accepted: 1 April 2020;

Published online: 14 April 2020

References

- Maier, S. A. *Plasmonics: Fundamentals and Applications* (Springer Science & Business Media, USA, 2007).
- Li, G. *et al.* A novel plasmonic resonance sensor based on an infrared perfect absorber. *J. Phys. Appl. Phys.* **45**, 205102 (2012).
- Rasooly, A. Surface plasmon resonance analysis of staphylococcal enterotoxin B in food. *J. Food Protect.* **64**, 37–43 (2001).
- Mauriz, E. *et al.* Multi-analyte SPR immunoassays for environmental biosensing of pesticides. *Anal. Bioanal. Chem.* **387**, 1449–1458 (2007).
- Chung, J. W., Kim, S. D., Bernhardt, R. & Pyun, J. C. Application of SPR biosensor for medical diagnostics of human hepatitis B virus (hHBV). *Sens. Actuators B* **111**, 416–422 (2005).
- Dai, X., Jiang, L. & Xiang, Y. Tunable optical bistability of dielectric/nonlinear graphene/dielectric heterostructures. *Opt. Express* **23**, 6497–6508 (2015).
- Hao, F. & Nordlander, P. Plasmonic coupling between a metallic nanosphere and a thin metallic wire. *Appl. Phys. Lett.* **89**, 103101 (2006).
- Chen, C. K., Heinz, T. F., Ricard, D. & Shen, Y. R. Surface-enhanced second-harmonic generation and Raman scattering. *Phys. Rev. B* **27**, 1965–1979 (1983).
- Wang, X. *et al.* Modulating plasmonic sensor with graphene-based silicon grating. *Plasmonics* **12**, 1725–1731 (2017).
- Nejat, M. & Nozhat, N. Design, theory and circuit model of wideband, tunable and polarization-insensitive terahertz absorber based on graphene. *IEEE Trans. Nanotech.* **18**, 684–690 (2019).
- Dai, D. & He, S. A silicon-based hybrid plasmonic waveguide with a metal cap for a nano-scale light confinement. *Opt. Express* **17**, 16646–16653 (2009).
- Pryce, I. M., Kelaita, Y. A., Aydin, K. & Atwater, H. A. Compliant metamaterials for resonantly enhanced infrared absorption spectroscopy and refractive index sensing. *ACS Nano* **5**, 8167–8174 (2011).
- Zhang, W. *et al.* Giant and uniform fluorescence enhancement over large areas using plasmonic nanodots in 3D resonant cavity nanoantenna by nanoimprinting. *Nanotechnology* **23**, 225301 (2012).
- Nejat, M. & Nozhat, N. Ultrasensitive THz refractive index sensor based on a controllable perfect MTM absorber. *IEEE Sens. J.* **19**, 10490–10497 (2019).
- Babaei, F., Javidnasab, M. & Rezaei, A. Supershape nanoparticle plasmons. *Plasmonics* **13**, 1491–1497 (2018).
- El Shamy, R. S., Khalil, D. & Swillam, M. A. Mid infrared optical gas sensor using plasmonic Mach-Zehnder interferometer. *Sci. Rep.* **10**, 1293 (2020).
- Rakhshani, M. R., Tavousi, A. & Mansouri-Birjandi, M. A. Design of a plasmonic sensor based on a square array of nanorods and two slot cavities with a high figure of merit for glucose concentration monitoring. *Appl. Opt.* **57**, 7798–7804 (2018).
- Jia, H. W. *et al.* Fabricating a long-range ordered 3D bimetallic nanoassembly with edge on substrate for highly sensitive SERS sensing of *Escherichia coli* bacteria. *Plasmonics* **10**, 1889–1894 (2015).
- Abbas, A., Fei, M., Tian, L. & Singamaneni, S. Trapping proteins within gold nanoparticle assemblies: dynamically tunable hot-spots for nanobiosensing. *Plasmonics* **8**, 537–544 (2013).
- Fritzsche, W. & Taton, T. A. Metal nanoparticles as labels for heterogeneous, chip-based DNA detection. *Nanotechnology* **14**, R63–R73 (2003).
- Zhang, D. *et al.* Streptavidin-enhanced surface plasmon resonance biosensor for highly sensitive and specific detection of microRNA. *Microchim. Acta.* **180**, 397–403 (2013).
- Takemura, K. *et al.* Versatility of a localized surface plasmon resonance-based gold nanoparticle-alloyed quantum dot nanobiosensor for immunofluorescence detection of viruses. *Biosens. Bioelectron.* **89**, 998–1005 (2017).
- Karlsson, R. & Stahlberg, R. Surface plasmon resonance detection and multipoint sensing for direct monitoring of interactions involving low-molecular-weight analytes and for determination of low affinities. *Anal. Biochem.* **228**, 274–280 (1995).
- Homola, J. Surface plasmon resonance sensors for detection of chemical and biological species. *Chem. Rev.* **108**, 462–493 (2008).
- Sun, D., Guo, T. & Guan, B. O. Label-free Detection of DNA Hybridization Using a Reflective Microfiber Bragg Grating Biosensor with Self-assembly Technique. *J. Light. Technol.* **35**, 3354–3359 (2017).
- Wu, F. *et al.* Layered material platform for surface plasmon resonance biosensing. *Sci. Rep.* **9**, 20286 (2019).
- Kim, H. M., Park, J. H. & Lee, S. K. Fiber optic sensor based on ZnO nanowires decorated by Au nanoparticles for improved plasmonic biosensor. *Sci. Rep.* **9**, 15605 (2019).
- Hameed, M. F. O., Saadeldin, A. S., Elkaramany, E. L. A. & Obayya, S. S. A. Label-Free Highly Sensitive Hybrid Plasmonic Biosensor for the Detection of DNA Hybridization. *J. Light. Technol.* **35**, 4851–4858 (2017).
- Islam, M. S. & Kouzani, A. Z. Simulation and Analysis of a Sub Wavelength Grating Based Multilayer Surface Plasmon Resonance Biosensor. *J. Light. Technol.* **31**, 1388–1398 (2013).
- Sun, X., Dai, D., Thyl'en, L. & Wosinski, L. High-sensitivity liquid refractive-index sensor based on a mach-zehnder interferometer with a double-slot hybrid plasmonic waveguide. *Optics Express* **23**, 25688–25699 (2015).
- Viphavakit, C. *et al.* Optimization of a horizontal slot WG biosensor to detect DNA hybridization. *Appl. Opt.* **54**, 4881–4888 (2015).
- Kabashin, A. V. *et al.* Plasmonic nanorod metamaterials for biosensing. *Nature Materials* **8**, 867–871 (2009).
- Withayachumnankul, W. *et al.* Metamaterial-based microfluidic sensor for dielectric characterization Sensors and Actuators A: Physical **189**, 233–237 (2013).
- Xu, Y., Wu, L. & Ang, L. K. MoS₂-based highly sensitive near-infrared surface plasmon resonance refractive index sensor. *IEEE J. Sel. Topics Quant. Electron.* **25**, 4600307 (2018).
- Kwon, M. S. Integrated plasmonic sensors. *Adv. Photon. OSA* (2014).
- Xie, Y. *et al.* A novel plasmonic sensor based on metal-insulator-metal waveguide with side-coupled hexagonal cavity. *IEEE Photonics J.* **7**, 1–12 (2015).
- Sun, T. *et al.* A compact optical switch via plasmonics of subwavelength circular-sharp hole arrays in metal films. *Ann. Phys.* **530**, 1700299 (2018).
- Johnson, P. B. & Christy, R. W. Optical constants of the noble metals. *Phys. Rev. B* **6**, 4370–4379 (1972).

39. Yang, J. *et al.* Broadband terahertz absorber based on multi-band continuous plasmon resonances in geometrically gradient dielectric-loaded graphene plasmon structure. *Sci. Rep.* **8**, 3239–3247 (2018).
40. Boyd R. W. *Nonlinear Optics* (Academic press, 3rd Ed. USA, 2008).
41. Liu, P. Y. *et al.* Cell refractive index for cell biology and disease diagnosis: past, present and future. *Lab. Chip* **16**, 634–644 (2016).
42. Balanis, C. A. *Advanced Engineering Electromagnetics*. (John Wiley & Sons, 2nd Ed., USA, 2012).
43. Xu, B., Gu, C., Li, Z. & Niu, Z. A novel structure for tunable terahertz absorber based on graphene. *Opt. Express* **21**, 23803–23811 (2013).
44. Wang, S. *et al.* The investigation of an LSPR refractive index sensor based on periodic gold nanorings array. *J. Physics D: Appl. Phys.* **51**, 045101 (2018).
45. Zhang, M. *et al.* Ultra-narrow band perfect absorbers based on Fano resonance in MIM metamaterials. *Opt. Commun.* **405**, 216–221 (2017).
46. Zhou, P. & Zheng, G. High-efficient light absorption of monolayer graphene via cylindrical dielectric arrays and the sensing application. *Opt. Mater.* **78**, 471–476 (2018).
47. Chen, J. *et al.* Dielectric waveguide-enhanced localized surface plasmon resonance refractive index sensing. *Opt. Mater. Express* **8**, 342–345 (2018).
48. Chen, J. *et al.* Optical cavity-enhanced localized surface plasmon resonance for high-quality sensing. *IEEE Photonics Technol. Lett.* **30**, 728–731 (2018).
49. Zafar, R. *et al.* Plasmonics-based refractive index Sensor for detection of hemoglobin concentration. *IEEE Sens. J.* **18**, 4372–4377 (2018).
50. Zhu, Y. *et al.* Magnetic plasmons in a simple metallic nanogroove array for refractive index sensing. *Opt. Express* **26**, 9148–9154 (2018).
51. Nurmohammadi, T., Abbasian, K. & Yadipour, R. Ultra-fast all-optical plasmonic switching in near infra-red spectrum using a Kerr nonlinear ring resonator. *Opt. Commun.* **410**, 142–147 (2018).
52. Singh, M. & Datta, A. Modeling of a vertical hybrid plasmonic switch with VO₂ Fin Bragg grating. *IEEE Photonics Technol. Lett.* **30**, 997–1000 (2018).
53. Singh, M. Design of hybrid multilayer plasmonic switch-cum-splitter with 90° bends. *Optik* **178**, 902–908 (2019).
54. Sun, X. *et al.* All-optical switching using a hybrid plasmonic donut resonator with photothermal absorber. *IEEE Photonics Technol. Lett.* **28**, 1609–1612 (2016).

Author contributions

This research was planned by M.N. and N.N. and they developed the analytical methods and analyzed the results. M.N. performed the numerical simulations and wrote the paper. All the authors reviewed the paper.

Competing interests

The authors declare no competing interests.

Additional information

Correspondence and requests for materials should be addressed to N.N.

Reprints and permissions information is available at www.nature.com/reprints.

Publisher's note Springer Nature remains neutral with regard to jurisdictional claims in published maps and institutional affiliations.



Open Access This article is licensed under a Creative Commons Attribution 4.0 International License, which permits use, sharing, adaptation, distribution and reproduction in any medium or format, as long as you give appropriate credit to the original author(s) and the source, provide a link to the Creative Commons license, and indicate if changes were made. The images or other third party material in this article are included in the article's Creative Commons license, unless indicated otherwise in a credit line to the material. If material is not included in the article's Creative Commons license and your intended use is not permitted by statutory regulation or exceeds the permitted use, you will need to obtain permission directly from the copyright holder. To view a copy of this license, visit <http://creativecommons.org/licenses/by/4.0/>.

© The Author(s) 2020